Water Research 263 (2024) 122195

Contents lists available at ScienceDirect

Water Research

journal homepage: www.elsevier.com/locate/watres

Sulfidation–reoxidation enhances heavy metal immobilization by vivianite

Zhangyi Xu [a], Ziyuan Huang [a], Han Li [a], Shishu Zhu [a], Zhenchao Lei [a], Chengshuai Liu [b,*], Fangyuan Meng [b], Jeng-Lung Chen [c], Tsung-Yi Chen [c], Chunhua Feng [a,*]

[a] Key Lab of Pollution Control and Ecosystem Restoration in Industry Clusters, Ministry of Education, School of Environment and Energy, South China University of Technology, Guangzhou 510006, PR China
[b] State Key Laboratory of Environmental Geochemistry, Institute of Geochemistry, Chinese Academy of Sciences, Guiyang 550081, PR China
[c] National Synchrotron Radiation Research Center, Hsinchu 30076, Taiwan, ROC

ARTICLE INFO

Keywords:
Iron cycle
Sulfur cycle
Heavy metal immobilization
Vivianite
Geochemistry

ABSTRACT

Iron minerals in nature are pivotal hosts for heavy metals, significantly influencing their geochemical cycling and eventual fate. It is generally accepted that, vivianite, a prevalent iron phosphate mineral in aquatic and terrestrial environments, exhibits a limited capacity for adsorbing cationic heavy metals. However, our study unveils a remarkable phenomenon that the synergistic interaction between sulfide (S^{2-}) and vivianite triggers an unexpected sulfidation–reoxidation process, enhancing the immobilization of heavy metals such as cadmium (Cd), copper (Cu), and zinc (Zn). For instance, the combination of vivianite and S^{2-} boosted the removal of Cd^{2+} from the aqueous phase under anaerobic conditions, and ensured the retention of Cd stabilized in the solid phase when shifted to aerobic conditions. It is intriguing to note that no discrete FeS formation was detected in the sulfidation phase, and the primary crystal structure of vivianite largely retained its integrity throughout the whole process. Detailed molecular-level investigations indicate that sulfidation predominantly targets the Fe(II) sites at the corners of the PO4 tetrahedron in vivianite. With the transition to aerobic conditions, the exothermic oxidation of CdS and the S sites in vivianite initiates, rendering it thermodynamically favorable for Cd to form multidentate coordination structures, predominantly through the Cd-O-P and Cd-O-Fe bonds. This mechanism elucidates how Cd is incorporated into the vivianite structure, highlighting a novel pathway for heavy metal immobilization via the sulfidation–reoxidation dynamics in iron phosphate minerals.

1. Introduction

Iron minerals are key in accommodating heavy metals within natural settings, and the study of their interaction mechanisms and geochemical implications has received significant interest (Alam and Elzinga, 2023; Brown et al., 1999; Huang et al., 2021a; Karna et al., 2021). Among these, vivianite ($Fe^{II}_3(PO_4)_2{\cdot}8H_2O$), recognized as the most common iron phosphate mineral formed anaerobically, has a widespread presence in various natural aquatic and terrestrial environments globally. The occurrence of vivianite is diverse, spanning from freshwater and coastal sediments (Rothe et al., 2016) to sinking particles and organic-rich soils (Frossard et al., 1996). It is even found in anthropogenic systems, such as sewage sludge, in the form of phosphorus recovery products (Saracanlao et al., 2024; Wilfert et al., 2016; Wu et al., 2021). Both chemically synthesized and biologically formed vivianite have demonstrated efficacy in immobilizing trace heavy metals, including arsenic (As) (Muehe et al., 2016), uranium (U) (Veeramani et al., 2011), mercury (Hg) (Etique et al., 2021), chromium (Cr) (Bae et al., 2018) and lead (Pb) (Liu and Zhao, 2007) through mechanisms such as adsorption, reduction, and co-precipitation. This ability of vivianite to bind heavy metals is of significant environmental importance, as it offers a natural method for mitigating heavy metal pollution in diverse ecosystems. However, the literature revealed little information regarding the immobilization of certain cationic heavy metals, specifically cadmium (Cd), copper (Cu), and zinc (Zn) by vivianite, attributed to its limited adsorption capacity for these metals. Our own experimental findings (see Fig. 1) also corroborated this, demonstrating that vivianite is a less effective agent for adsorbing these heavy metals. Factors such as the crystal lattice structure, surface charge, and surface area of vivianite appear to be less conducive to the incorporation or adsorption of them (Hong et al., 2023; Muehe et al., 2016; Wang et al., 2023a), thereby limiting its capacity in controlling the environmental impact of these metals.

Sulfide (S^{2-}) is also commonly available in anaerobic environments, resulting from the metabolic reduction of sulfate (SO_4^{2-}) that is coupled

* Corresponding authors.
E-mail addresses: liuchengshuai@vip.gyig.ac.cn (C. Liu), chfeng@scut.edu.cn (C. Feng).

https://doi.org/10.1016/j.watres.2024.122195
Received 9 March 2024; Received in revised form 24 July 2024; Accepted 30 July 2024
Available online 31 July 2024

with the oxidation of organic carbon (Sun et al., 2023; Wang et al., 2023b, 2023c). In general, fluctuations in redox conditions frequently induce cycles of iron (Fe) and sulfur (S), which in turn can drastically alter the types of Fe minerals present as well as the fate of heavy metals (Brown et al., 1999; Eitel and Taillefert, 2017; Huang et al., 2021a; Tagliabue et al., 2017). Typically, a shift from anaerobic to aerobic conditions results in the dissolution of heavy metal sulfides and Fe sulfides, which could increase the mobility of heavy metals, potentially leading to environmental contamination. However, in our study, we observe an unexpected phenomenon that triggers our interest: simulations of the coexistence of vivianite with heavy metals under natural anoxic conditions (Bogush et al., 2022; Wang et al., 2023a) indicate that the presence of S^{2-} potentially enhanced the immobilization of Cd, Cu, and Zn through a sulfidation–reoxidation process. This finding highlights complex interactions between vivianite, S^{2-}, and metal ions, suggesting that the sulfidation–reoxidation process alters the chemical environment or the properties of vivianite, thus enhancing its capacity to bind with heavy metals. Such dynamic interactions offer new insights into the geochemical behavior of heavy metals in environments where both vivianite and S^{2-}coexist.

Therefore, taking Cd as an example, the primary objective of our study is to thoroughly investigate and understand the enhancement of Cd sequestration by vivianite via sulfidation–reoxidation. We aim to elucidate the molecular-level mechanisms underlying this phenomenon, exploring how the synergistic interaction between S^{2-} and vivianite leads to a significant increase in the immobilization capacity for Cd. By employing advanced analytical and spectroscopic techniques, we intend to examine the changes in the chemical structure and surface properties of vivianite during the sulfidation–reoxidation process. This investigation will not only deepen our understanding of the immobilization processes of heavy metals in natural environments but also potentially pave the way for developing more effective strategies for environmental remediation involving cationic heavy metal pollutants.

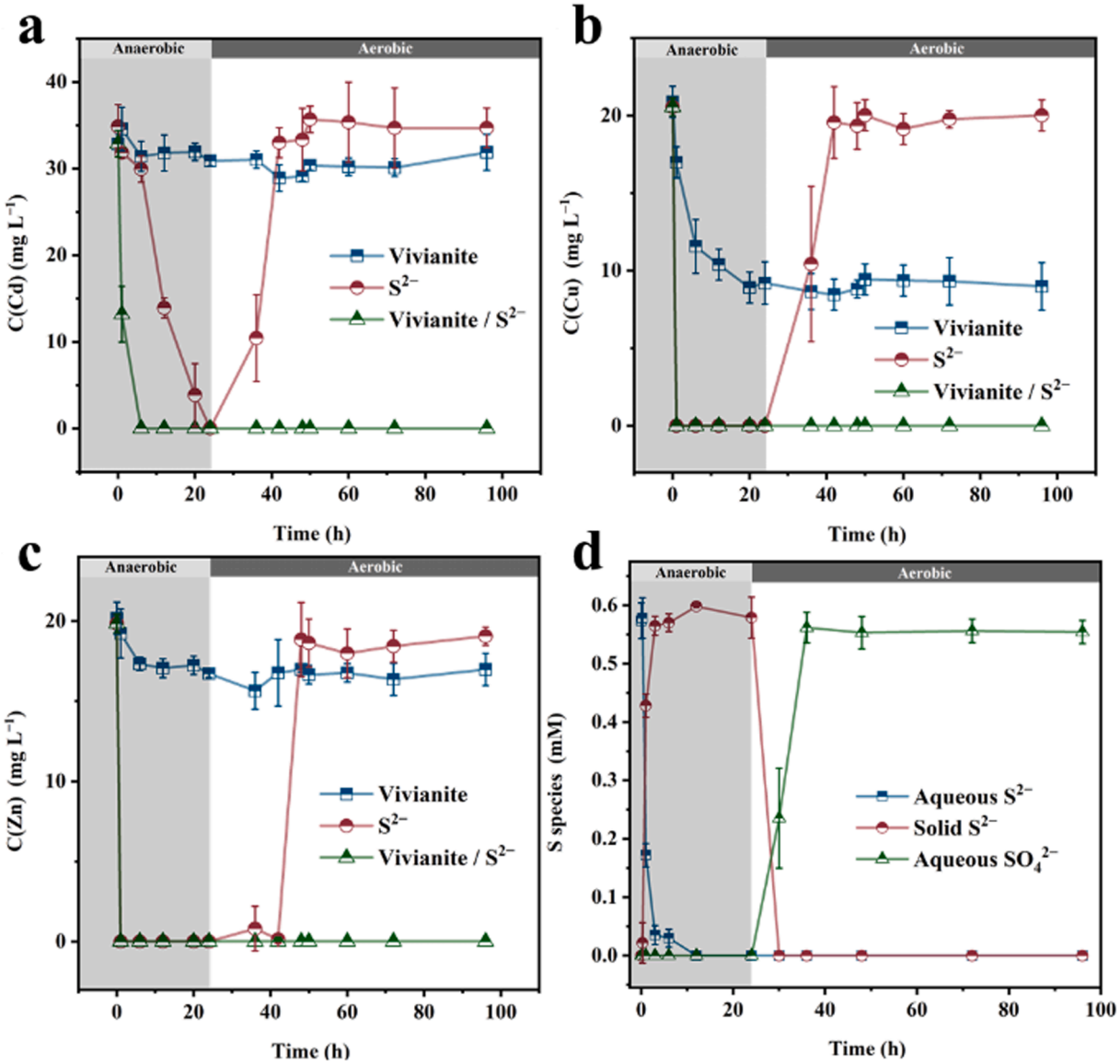

Fig. 1. Time courses of dissolved (a) Cd^{2+}, (b) Cu^{2+}, and (c) Zn^{2+} concentrations under various treatments: S^{2-} alone, vivianite alone, and a combination of both. (d) Time courses of concentrations of different S species in the combined vivianite/Cd^{2+} system. Experimental conditions: [vivianite] = 0.4 g L^{-1}, [Cd^{2+}] = [Cu^{2+}] = [Zn^{2+}] = 0.3 mM, [S^{2-}] = 600 μM, and pH = 6.5.

2. Materials and methods

2.1. Chemicals and reagents

Ammonium ferrous sulfate hexahydrate ($Fe(NH_4)_2SO_4{\cdot}6H_2O$, 99 %), anhydrous sodium acetate (CH_3OONa, > 99 %), anhydrous dibasic sodium phosphate (Na_2HPO_4, 99 %,), cadmium sulfate ($CdSO_4$, >98.0 %), zinc sulfate ($ZnSO_4$, >98.0 %), copper sulfate ($CuSO_4$, >98.0 %), sodium sulfide nonahydrate ($Na_2S{\cdot}9H_2O$, 99 %), sodium hydroxide (NaOH, >97.0 %), 2-(N-morpholino) ethanesulfonic acid (MES, ≥99.5 %) were purchased from Aladdin Industrial Corporation (Shanghai, China). All solutions were prepared from analytical grade chemicals, N_2-outgassed doubly deionized (DDI) water (Milli-Q, Millipore, 18.2 MΩ cm).

2.2. Chemical synthesis

The synthesis of vivianite was conducted within an anoxic chamber (MBraun, UNIlab Plus) equipped with an N_2 atmosphere, ensuring an ultra-low oxygen concentration of less than 1 ppm (v/v). The process was performed at a controlled temperature of 45 °C. The synthesis protocol involved the precipitation of vivianite from aqueous solutions containing 1 mM $(NH_4)_2HPO_4$ and 1 mM $FeSO_4{\cdot}7H_2O$. This approach was carefully designed to maintain a slight excess of phosphate, aiming to effectively scavenge all the Fe^{2+} ions present in the solution (Bae et al., 2018). The initial pH of the solution, which was slightly acidic, was adjusted to 7.0 ± 0.2 by dropwise addition of 4 M NaOH solution. To safeguard against light exposure sensitivity, the synthesis was carried out in amber glass flasks. The procedures for synthesis of FeS and CdS are detailed in Text S1.

2.3. Sulfidation–reoxidation experiments

Sulfidation experiments were performed under anoxic conditions in a 50 mM MES buffer (pH 6.5) solution containing 0.4 g L^{-1} vivianite, 0.3 mM heavy metals (Cd^{2+}, Cu^{2+}, Zn^{2+}), and 600 μM Na_2S (He et al., 2019). It should be noted that a pH of 6.5 is close to the neutral pH of many natural water bodies, providing understanding of how sulfidation processes might occur in real-world environments (Qin et al., 2022). The vivianite concentration of 0.4 g L^{-1} is consistent with levels detected in anaerobic environments (Cosmidis et al., 2014), and the concentration of cationic heavy metals at 0.3 mM falls within the range typically found in acid mine drainage (Pan et al., 2023). The concentration of S^{2-} is taken as 0.6 mM, as it ranges from 0.4 to 0.8 mM in sediment and soil pore water (Xiong et al., 2019). The experiments were conducted in 250 mL glass serum bottles sealed with rubber stoppers, ensuring S loss due to volatilization remained below 5 %. This was confirmed by measuring the concentrations of different S species in both the liquid and solid phases throughout the experiments. The bottles, containing various suspensions and respective treatments, were agitated in the dark on a magnetic stirrer at 100 rpm and 25 °C. After 24 h, aliquots were drawn from the bottles and filtered through 0.02 μm poly(ether sulfone) (PES) membrane filters in the glovebox, facilitating the subsequent assessment of dissolved total iron (Fe_{tot}), Fe(II), and heavy metal concentrations. These aliquots then underwent ultracentrifugation at 40,000 rpm and were freeze-dried to harvest the solid phase. The remaining suspensions in the bottles were shielded with sterile filter membranes to enable air exchange while minimizing solution evaporation. These bottles were then agitated in the dark on a magnetic stirrer at the same settings. After a 3-day air exposure, both the aqueous and solid phases were collected, processed, and analyzed using the methods previously mentioned. All experiments were conducted in triplicate.

2.4. Characterizations and analyses

The concentrations of dissolved heavy metals (Cd^{2+}, Cu^{2+}, Zn^{2+}) in the batch experiments were measured using an atomic absorption spectrometer (AAS, PinAAcle 900T, PerkinElmer, USA). The procedures for measuring adsorbed and structural Cd followed previously established procedures (Qiu et al., 2023). Briefly, vivianite-bound Cd was analyzed by first freeze-drying the residual solid. To assess the adsorbed Cd, 0.4 M HCl was added to the dried solid, which was then agitated at 200 rpm for 30 min. The supernatant was collected to measure the adsorbed Cd content. The remaining solid was treated with 4 M HCl and similarly agitated for 30 min. The supernatant from this mixture was then collected via centrifugation to determine the structural Cd content. Fe(II) and Fe_{tot} contents in the aqueous samples were quantified via the Ferrozine analysis (Huang et al., 2023). The concentration of aqueous S^{2-} was measured using the methylene blue method (He et al., 2019), and the concentration of aqueous SO_4^{2-} was determined via ion chromatography (ICS-5000, Dionex, USA). The solid-phase S^{2-} and solid SO_4^{2-} contents were quantified by dissolving the solid with 0.4 mM HCl, followed by measurement of their concentrations in the filtrate under anaerobic conditions. The redox potential of the solution was determined using a Thermo RDO portable instrument (Scientific Orion Star A221, USA). The surface morphology of the solid samples was examined using scanning electron microscopy (SEM, Merlin, Zeiss Co., Germany). Mineral phases within selected solid samples were identified with an X-ray diffractometer (XRD, X'Pert PRO MRD, PANalytical, Holland, Germany). Diffractograms were obtained over a 2θ range of 10−70°, employing a step size of 0.02° and a scan rate of 5° per min. Fourier transform infrared spectra (FTIR, VERTEX 33, Bruker, Germany) were measured in the absorbance mode in the range of 400–4500 cm^{-1} with a spectral resolution of 4 cm^{-1}. Mössbauer spectra were recorded at 293 K in transmission mode using a WSS-10 Mössbauer spectrometer (WissEL GmbH, Germany), coupled with a closed-cycle cryostat (SHI-850, Janis Research Co., Wilmington, MA, USA). The velocity scale for the Mössbauer spectra was calibrated using α-iron as a standard. The Nernst equations used for modelling the Pourbaix diagrams to predict the stability of different S species are listed in Text S2.

X-ray adsorption spectra (XAS) for the Fe (6931 eV) and Cd K-edges (26,518 eV) were captured in transmission mode at the beamlines BL17C and BL01C of the Taiwan Synchrotron Radiation Lightsource (TSRL), respectively. The analysis of the XAS data was conducted using the Demeter software package (Ravel and Newville, 2005). Specifically, the XAS data were treated in Athena (version 0.9.26) for background subtraction, pre-edge line, and post-edge line calibrations. The obtained EXAFS data, prior to Fourier transformation, were weighted by k3. The amplitude reduction factor was fixed at 0.926 for all Fe K-edge fits, and the amplitude reduction factor was fixed at 0.9 for all Cd K-edge fits. The data, after undergoing Fourier transformation into R-space, were fitted using the Artemis component of the software, which provided refined values for the distance to the scattering atom (R), the mean-squared displacement (σ2), and the coordination number (CN) through a least-squares refinement approach. Theoretical scattering phases and amplitudes were calculated using the crystal structure of vivianite $[Fe_3(PO_4)_2{\cdot}8H_2O]$ and cadmium iron diphosphate $[Cd_{2.5}FeO_{14}P_4]$ to model possible Fe-O, Fe-P, and Fe-Cd interactions (Dormann et al., 1982; ElBelghitti et al., 1994). CdS and $Cd_{2.5}FeO_{14}P_4$ were used to model Cd-S, Cd-O, and Cd-Fe interactions (Mueller and Loeffler, 1933). The wavelet transform of the EXAFS spectra was analyzed using Continuous Cauchy mother wavelets (Funke et al., 2007). This analysis was executed by the HAMA Fortran program, employing a morlet mother wavelet function with parameter settings of $\kappa = 10$ and $\sigma = 1$, to unravel intricate details in the EXAFS spectra.

2.5. Computational details

Density functional theory (DFT) calculations were carried out using Materials Studio 2020, with the Perdew–Burke–Ernzerhof (PBE) exchange-correlational functional under the generalized gradient approximation (GGA) framework (Delley, 2000). The Dmol3 tools within the software package were specifically utilized for these

computations (Delley, 1990). In this study, the valence electron configurations for the elements involved were carefully chosen as $4s^2 3d^6$ for Fe, $3s^2 3p^3$ for P, $2s^2 2p^4$ for O, $3s^2 3p^4$ for S, and $4d^{10} 5s^2$ for Cd. Electronic energy was considered self-consistent when the energy change was less than 10^{-6} eV, and the maximum displacement tolerance was 0.005 Å. Based on the crystal cell size of minerals, for the bulk structure of vivianite and other small-molecular structures, a ($17 \times 17 \times 17$) mesh and a ($7 \times 9 \times 4$) mesh were employed for reciprocal space sampling, respectively (Momma and Izumi, 2008).

3. Results and discussion

3.1. Synergistic role of vivianite and the sulfidation–reoxidation process in enhancing cationic heavy metal immobilization

In Fig. 1a, the comparative study on the removal of Cd^{2+} during the anaerobic-aerobic transition revealed distinct outcomes under various treatments: S^{2-} alone, vivianite alone, and a combination of both. The presence of vivianite alone resulted in minimal disappearance of Cd^{2+} (10 % removal within 24 h), which is attributed to its limited adsorption capacity, likely due to scarce phosphate active sites and a low surface area (Pinto et al., 2014). XRD analysis displayed no structural changes in vivianite before and after Cd^{2+} adsorption, as illustrated in Fig. S1. Conversely, S^{2-} effectively precipitates Cd^{2+} during anaerobic conditions (100 % removal within 24 h) but led to re-release of Cd^{2+} upon reoxidation, suggesting the limited role of S^{2-} in immobilization. Notably, the combined use of vivianite and S^{2-} significantly enhanced Cd^{2+} removal (100 % removal within 6 h), outperforming the individual treatments, and prevented Cd^{2+} re-release during oxidation, indicating a synergistic effect. This finding, mirrored in analogous experiments with Cu^{2+} (Fig. 1b) and Zn^{2+}(Fig. 1c), underscores the potential of integrating vivianite with the sulfidation−reoxidation process for more effective heavy metal immobilization in fluctuating anaerobic-aerobic environments. Similar phenomenon was observed at low-concentration S^{2-} (Fig. S2); however, the degree of Cd^{2+} immobilization in this scenario was less than that observed with a higher S^{2-} level. Multiple-cycle experiments showed that no Cd^{2+} was released from the solid to the liquid phase, indicating the high stability of Cd^{2+} immobilization throughout the sulfurization-reoxidation process (Fig. S3).

The variations in the concentrations of different S components during the sulfidation−reoxidation process closely linked with the fate of Cd in the system involving S^{2-} and vivianite. As shown in Fig. 1d, the anaerobic phase witnessed the transfer of S^{2-} from the liquid to the solid phase within 6 h, primarily through the precipitation of Cd^{2+} and the sulfidation of Fe(II) in vivianite. In the subsequent aerobic phase, S^{2-} in the solid form quickly oxidized into SO_4^{2-}, leading to a remarkable dissolution of S (92 %) into the solution over a 12-h reaction, with the residual S adhering to the vivianite surface, potentially in an adsorbed form. The concentrations of solid-phase and liquid-phase phosphates were also monitored. The results indicate that no phosphorus species were released into the liquid during the sulfidation−reoxidation process (Fig. S4), implying that the replacement of the phosphate sites in vivianite by S atoms rarely occurred. As shown in Fig. S5, the redox potential of the solution gradually increased from −284 mV (*vs.* NHE) to approximately −20 mV (*vs.* NHE), as S^{2-} was consumed during sulfidation, and it further rose to 60 mV (*vs.* NHE) under aerobic conditions. No aqueous Fe(II) or Fe(III) species were detected throughout the process (Fig. S6), indicating minimal Fe(II) oxidation and Fe(III) dissolution across various redox potentials. This also suggests that the incorporation of Cd into vivianite likely did not displace Fe from its structure. The molecule-level mechanisms will be further elucidated in the following sections.

To investigate the impact of the sulfidation−reoxidation process on Cd speciation and mobility, the proportions of dissolved, adsorbed, and structural Cd were measured over time in the treatment involving both S^{2-} and vivianite (Fig. 2a). By the end of the anaerobic phase, all Cd in the liquid phase transitioned to the solid phase, with 70 % existing as adsorbed Cd. It is noticeable that the aerobic phase did not result in the release of dissolved Cd; instead, it led to an increased proportion of structural Cd over time, indicating a robust interaction between Cd and the Fe minerals. This shift towards a greater fraction of structural Cd suggests a reduced risk of heavy metal dissolution, which is desirable for heavy metal passivation.

The XRD patterns of solids, in the presence of both S^{2-} and vivianite, were recorded at various intervals, as depicted in Fig. 2b. After 24 h of the anaerobic phase, distinct new peaks corresponding to greenockite (CdS) were evident (Huang et al., 2021b). Concurrently, there was a distinct decrease in the intensity of the XRD peaks of vivianite, implying that Fe(II) in vivianite interacted with S^{2-} to a certain extent. However, the absence of peaks related to FeS (Figs. S7 and 2b) suggests that no distinct crystalline FeS phase formed. Upon transitioning to aerobic conditions, the XRD patterns specific to CdS vanished, and the intensity of vivianite-associated peaks increased over time. It is important to note that no additional Fe mineral phases were detected throughout the entire sulfidation−reoxidation process. This observation indicates that the primary crystal structure of vivianite remained largely intact, even in the dynamically changing anaerobic-aerobic environments. Fig. S8 displays SEM images of solid samples taken at various stages, all showing the characteristic morphology of vivianite, which is defined by its distinct crystalline structure with smooth, faceted surfaces, and a typical layered arrangement. Detailed energy dispersive spectroscopy (EDS) analysis indicates that the sulfidation phase caused the incorporation of Cd and S elements within the solid matrix. Interestingly, the shift from anaerobic to aerobic conditions resulted in the disappearance of S elements from the internal structure of the solids, while Cd remained immobilized. This is consistent with the results from the Cd speciation analysis, manifesting the effectiveness in altering the elemental composition while retaining Cd within the solid structure.

3.2. Mechanistic insight into Cd immobilization by vivianite via sulfidation−reoxidation

Pourbaix diagrams, also known as E_h-pH diagrams, are instrumental in environmental science for predicting the thermodynamic stability of species in aqueous solutions (Yiming et al., 2018). They were used to determine the stability of S species in anaerobic environments (with E_h ranging from −0.2 to −0.8 V *vs.* NHE) and at pH 6.5, which were affected by the presence of Fe(II) and Cd^{2+}. As shown in Fig. 3a, under these specific conditions, CdS emerges as the predominant species. The introduction of Fe(II) leads to a portion of S binding with Fe, resulting in the formation of FeS. This finding is crucial in explaining the co-presence of CdS and Fe(II)-S in the treatment involving both S^{2-} and vivianite at the end of the anaerobic phase. However, intriguingly, XRD characterization indicates the absence of a crystalline FeS phase in these samples; this raises further questions about the interaction between S^{2-} and vivianite in anaerobic environments, a topic that warrants deeper exploration.

The Mössbauer spectroscopy method, with its ability to discern and quantify different Fe species at a molecular level, was employed to elucidate the binding between S^{2-} and vivianite (Chen et al., 2017). Fig. 3c shows the room-temperature Mössbauer results of samples from different treatment phases and Table S1 summarizes the detailed parameters for the fitting of Mössbauer spectra. In the pristine vivianite sample, the D_1 (Fe(II) positioned at the edges of the PO4 tetrahedron in vivianite) showed higher isomer shift (IS) and quadrupole splitting (QS) values compared to D_2 (Fe(II) located at the corners of the PO4 tetrahedron in vivianite), occupying a more substantial portion relative to Fe (Dyar et al., 2014). During the sulfidation process under anaerobic environments, the content of D_1 Fe(II) remained relatively unchanged, whereas the proportion of D_2 Fe(II) transitioned into a new D4 Fe(II) component. The newly emerged D_4 Fe(II) is presumed to be partially

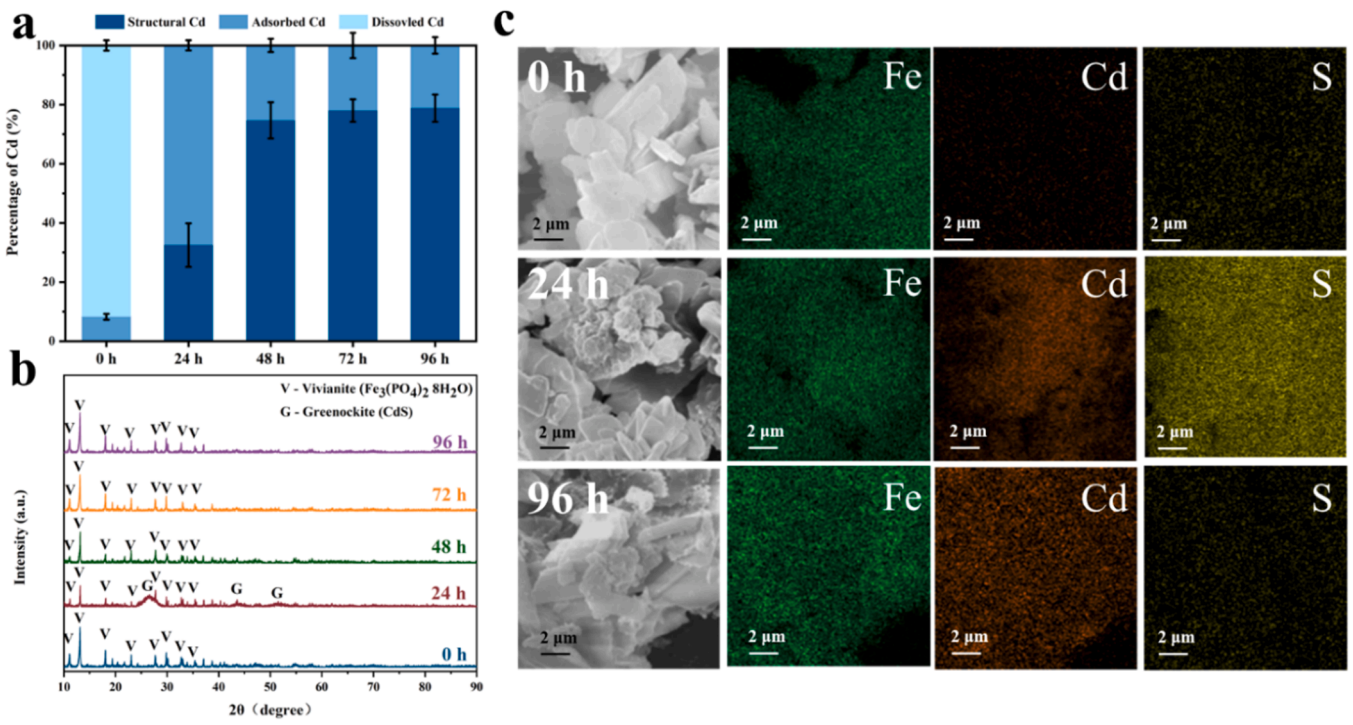

Fig. 2. Time courses of (a) Cd relative fraction, and (b) XRD patterns and (c) elemental mapping images of the solid phase during the sulfidation–reoxidation process.

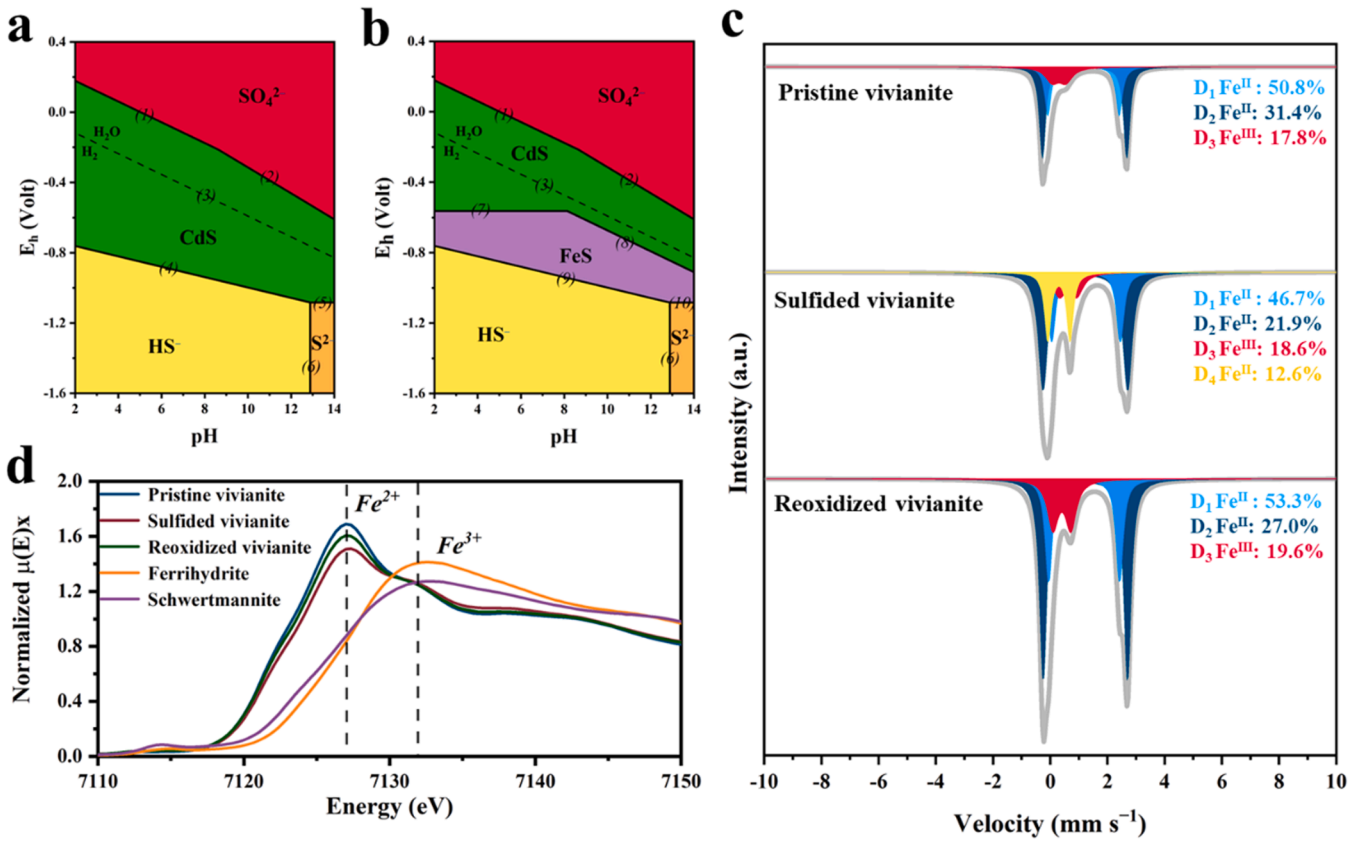

Fig. 3. E_h–pH diagrams of S species (a) without and (b) with the involvement of Fe(II). (c) 298 K Mössbauer spectra and (d) Fe K-edge XANES spectra of the solid phase in the combined vivianite/Cd^{2+} system during the sulfidation–reoxidation process.

S-bound (Cheng et al., 2020), indicating that sulfidation occurred selectively at the Fe(II) sites at the corners of the PO4 tetrahedron. Furthermore, the appearance of the D_4 doublet in the Mössbauer spectrum of sulfided vivianite, with a QS of 0.6, contradicts the expected low spin state of Fe in FeS (Schröder et al., 2020). This implies that the sulfided Fe(II) sites were likely coordinated with elements besides S, an aspect that highlights the complexity of the sulfidation process in the vivianite structure. During the oxidation phase, the portion indicative of Fe-S bonding (D4) observed during sulfidation reverted entirely to the relative area of D2 Fe(II), signifying a full oxidation back to its original state. It is observable that the proportion of D3 Fe(III), frequently identified as a doublet and potentially corresponding to metavivianite (Etique et al., 2021), maintained a relatively steady level throughout the sulfidation−reoxidation process. This observation implies that there was no significant oxidation of Fe(II) to Fe(III) or reduction of Fe(III) to Fe(II) during the sequence of reactions.

To corroborate this observation, acid dissolution experiments were performed on the solid samples collected at different intervals of the experiment to measure the Fe(II) and Fe(III) contents. The results confirm that the Fe(III) levels in the solid were pretty low and there were only minimal variations (< 10 %) in the Fe(II) concentrations over the entire duration of the experiment (Fig. S6). Moreover, the application of X-ray absorption near-edge structure (XANES) spectroscopy provides further insights into the oxidation state of Fe (Liang et al., 2020). The XANES spectra displayed no apparent shift in the energy of the peak associated with Fe(II) throughout the experimental process. This observation is of particular interest, as it starkly contrasts with the spectral signatures typically attributed to Fe(III) compounds (*e.g.*, ferrihydrite or schwertmannite). The absence of a significant energy shift in the XANES spectra strongly suggests that the sulfidation−reoxidation process did not induce any oxidation of Fe(II) or reduction of Fe(III). These findings collectively demonstrate the remarkable stability of the Fe species, particularly Fe(II), in the vivianite structure throughout the sulfidation−reoxidation process, emphasizing the resilience of the vivianite matrix against redox transformations under these specific experimental conditions.

To better understand the local Fe coordination environment within vivianite, the Fe k^2-weighted extended X-ray absorption fine structure (EXAFS) spectra (Fig. S9) were examined for insights into Fe bonding, CN, and distances to neighboring atoms. Fig. 4a indicates that, after sulfidation, the first shell's peak shifted towards a higher R value, but reverted to its original position after reoxidation. The second shell's peak also shifted rightward upon reoxidation, suggesting possible changes in molecular bond distances or atom substitutions (Szeto et al., 2018). Detailed chemical bond changes during the sulfidation−reoxidation process were uncovered by fitting the EXAFS data, with parameters at the Fe K-edge for various samples outlined in Table S2. In the first shell of the vivianite molecule, the main peak was exclusively attributed to the Fe-O bond with a length of 2.08 Å and CN ranging between 5 and 6, which are in line with the average CN observed at the two Fe sites in vivianite (Li et al., 2015). The second shell showed the Fe-P coordination pathway, which is facilitated through an Fe-O-P bond with an average length of 3.2 Å, consistent with literature reports (Bae et al., 2018). During the sulfidation phase, the primary peak of the first shell exhibited an increase of about 0.2 Å in the R value, indicating S atoms substitution for O atoms. This change partially shifted the Fe-O bond (average length 2.03 Å) to the Fe-S bond (average length 2.31 Å). As S^{2-} concentration increased, the EXAFS data revealed an enhanced sulfidation effect, significantly increasing CN of S on Fe sites (from 0.9 to 2.8), while keeping the total CN close to the original Fe-O count in that shell (CN ≈ 5.1). Concurrently, the Fe-P coordination in the second shell remained stable in the CN and distance, consistent with Mössbauer data and suggesting that sulfidation was confined within the vivianite molecule. During the reoxidation stage, the primary peak of the first shell in vivianite shifted left back to 2.01 Å, indicative of oxidation of Fe-S to Fe-O, thereby returning the first shell's structure to its original state. To address potential biases from k-value selection in Fourier transformation, a morlet wavelet function was used for K-edge data analysis (Rastegari et al., 2022). The wavelet analysis (Fig. 4b) showed Fe-P signals in the second shell of initial vivianite (R ≈ 2.7 Å, K

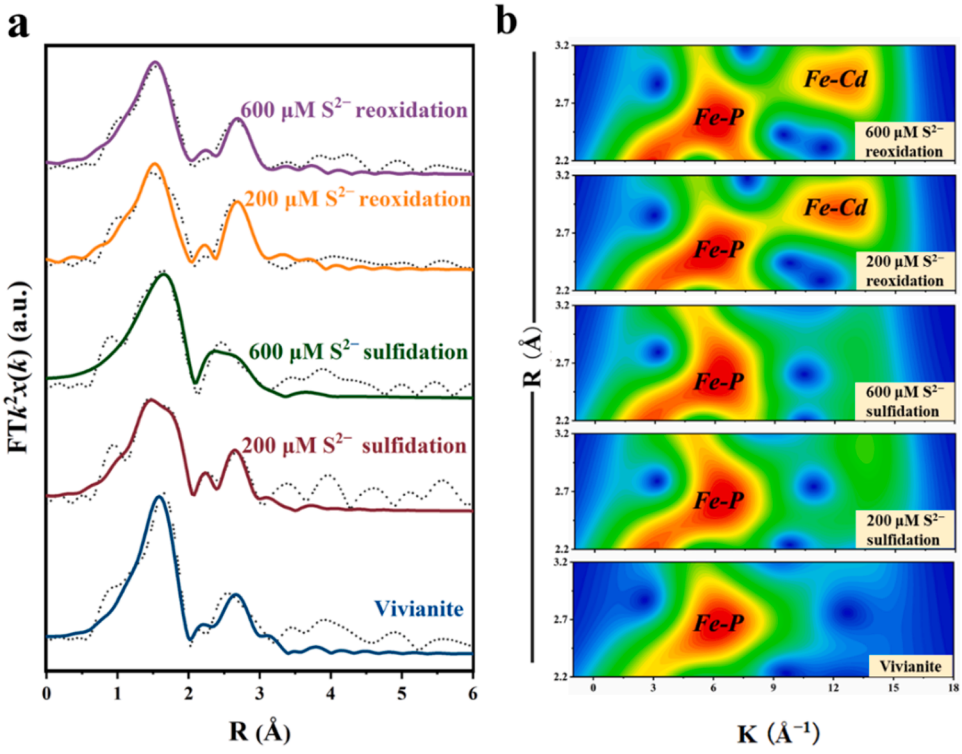

Fig. 4. (a) Fourier transforms of Fe k^2-weighted EXAFS spectra and (b) their corresponding Morlet wavelet transforms of the solid phase in the combined vivianite/Cd^{2+} system during the sulfidation–reoxidation process.

range 3–9 $Å^{-1}$), indicative of Fe-O-P bond (Zhang et al., 2021). After sulfidation−reoxidation in the vivianite/Cd^{2+} system, new signals appeared at higher R (≈ 2.9 Å) and K (≈ 12 $Å^{-1}$) values, suggesting the formation of Fe coordination pathways with larger atoms, ascribed to Fe-O-Cd bond (Yu and Fein 2015). This observation is in good agreement with the findings from the Fourier transformation. As shown in Fig. 4 and Table S2, there was rightward shift in the R value of the second shell in vivianite, and the Fe-Cd coordination distance was longer than that of Fe-P, being approximately 3.3 Å as compared to 3.2 Å. Moreover, an increase in S^{2-} concentration resulted in a higher CN of the Fe-O-Cd bond.

The coordination environment of Cd during the sulfidation−reoxidation process was also analyzed based on the EXAFS spectra and their Fourier transforms (Fig. 5a and b). In the S-free group (vivianite + Cd), the R-edge showed a peak at a low R value. However, after the sulfidation process, there was a significant rightward shift of 0.4 Å in the peak, suggesting a likely substitution of the coordination pathway (Cutsail et al., 2018). Compared to the sulfidized experimental group, the R-edge of the reoxidized vivianite displayed a noticeable leftward shift in the first shell peak, indicating the coordination of Cd with atoms of lower mass (Zhou et al., 2023). The reoxidized group, as compared to the original S-free group, showed a higher peak in the first shell and the emergence of a new peak in the second shell, both implying a more stable immobilization of Cd in vivianite (Martinie et al., 2017).

To clarify the specific mechanisms of this process, a Fourier fitting of the original EXAFS data was conducted. From the post-fitting k-space spectra, a noticeable peak shift was observed during the sulfidation stage, indicating changes in the Cd coordination environment. The highest peak intensity in the reoxidation group corresponded to the highest CN of Cd observed in the process. Compared to the signals obtained from the S-free conditions, more distinct waveforms appeared in the corresponding high k-value region (> 8 $Å^{-1}$), suggesting the formation of new coordination paths with larger R values (Yin et al., 2019). Table S3 shows that, in the case of S-free group, it is believed that the primary binding mode was through Cd-O coordination (R = 2.2 Å) at the phosphate sites on the vivianite surface. This is also confirmed by FTIR experiments, which indicate that the vibrations of surface-active phosphate (P-OH, P-$(OFe)_2$, and PO_2^-) weakened, and the symmetric stretching of PO_3 and PO_2 increased after Cd^{2+} adsorption (Fig. S10). These changes suggest stronger Cd-O-P bonds, intensifying with higher

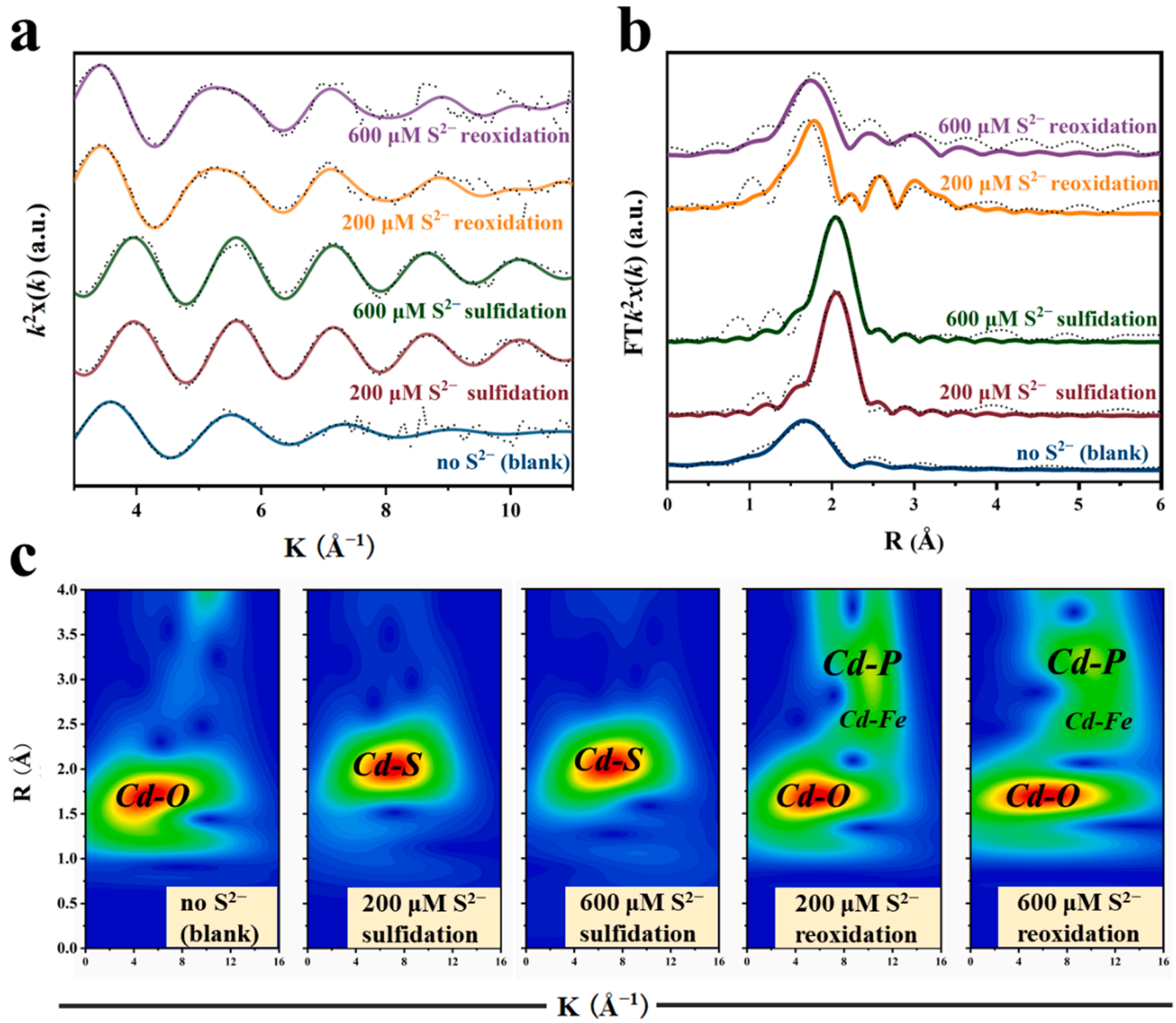

Fig. 5. (a) Cd k^2-weighted EXAFS spectra and their corresponding (b) Fourier transforms and (c) Morlet wavelet transforms of the solid phase in the combined vivianite/Cd^{2+} system during the sulfidation–reoxidation process.

Cd^{2+} concentrations. Under sulfidation conditions, Cd^{2+} directly precipitates with S^{2-}, with the main coordination form being Cd-S with a bond length of 3.1 Å. Considering the corrections for the R values in the Fourier equation, it is determined that the shift from Cd-O to Cd-S coordination was the reason for the main peak's rightward shift. Under sulfidation conditions, the CN of Cd-S was close to 4, consistent with the coordination structure of CdS crystals (Sun et al., 2020) and aligning with the CdS crystallographic information confirmed by XRD. Upon reoxidation of the system, the Cd coordination reverted to Cd-O with a distinct increase in CN (from 4.8 to approximately 5.9), and the Cd-Fe and Cd-P coordination pathways emerged in the second shell, fully illustrating a more stable incorporation of Cd in the coordination environment. In different groups with varying S^{2-}contents, a consistent CN of Cd-Fe (0.7) and Cd-P (2.0) was observed, indicating that the intensification of sulfidation did not affect the coordination environment of Cd. The higher CN of Cd-P compared to Cd-Fe suggests that the formation of Cd-O-P bonds contributed significantly to the coordination-based immobilization.

The Morlet wavelet transform results of EXAFS (Fig. 5c) show that under S-free conditions, a unique strong response signal of Cd-O was present near a k-value of 5 $Å^{-1}$. Compared to the phosphate on the vivianite surface, S^{2-} exhibited a stronger binding affinity for Cd^{2+}. As a result, S^{2-} occupied all of Cd coordination sites during sulfidation, contributing to all response signals with high k-values, which represent larger molecular weights. After the complete oxidation of S^{2-} in the system, the coordination of Cd in the wavelet space shifted back to the Cd-O region, with new response signals of Cd-Fe and Cd-P appearing in the high R and high k-value regions, forming internal Cd-O-Fe and Cd-O-P bonds (Cutsail et al., 2018). The consistency between the wavelet transformation and spectral fitting results validates the observed enhancement and transformation in the coordination form of Cd during the whole process.

3.3. Theoretical analysis of the reaction pathways involving Cd, sulfide, and vivianite

Utilizing the bond length data derived from EXAFS Fourier fitting, a molecular model of vivianite was developed, and DFT calculations were conducted to facilitate the simulation of potential reaction pathways throughout the sulfidation–reoxidation process. As shown in Fig. 6, the molecular structure of vivianite features Fe sites that interact with the PO4 tetrahedron in two distinct manners: Fe sites forming shared corners, termed Fe(II)-A sites, and those creating shared edges, referred to as Fe(II)-B sites (Pinto et al., 2014). In the sulfidation phase (Path I), it is hypothesized that S atoms could replace O atoms adjacent to either A sites or B sites. Molecular configurations representing this substitution were crafted, and the energy barriers for these reactions were quantified. The results suggest that the sulfidation of both Fe sites occurs spontaneously. Nevertheless, it is noted that the substitution of Fe-O with S at the A sites exhibits a lower reaction energy barrier compared

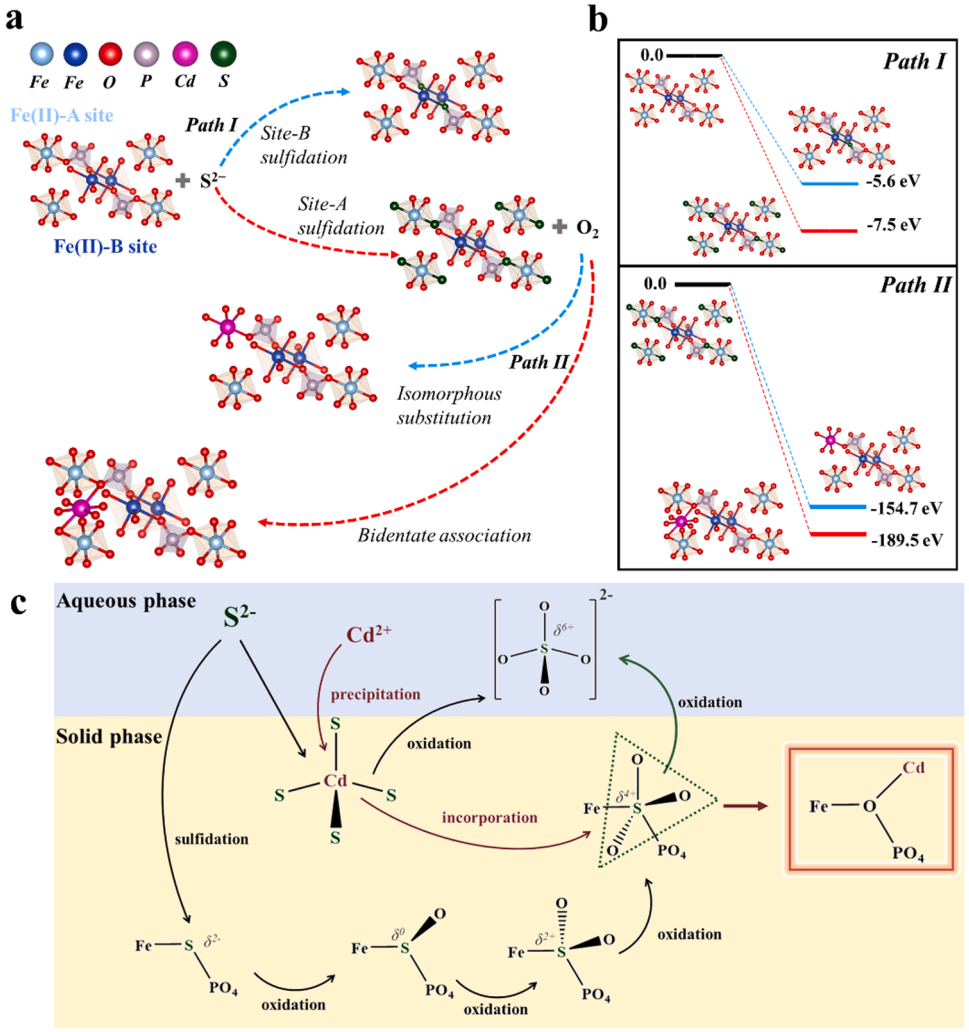

Fig. 6. (a) Proposed reaction pathways, (b) theoretical calculations of the energy barriers of specific pathways, and (c) illustration of behavior and fate of S and Cd species in the aqueous phase and the solid phase during the sulfidation–reoxidation process.

to the B sites. This suggests a preferential replacement by the less electronegative S, which selectively targets O atoms that present lesser steric hindrance, leading to a spontaneous substitution process.

During the reoxidation process (Path II), the exothermic oxidation of CdS and the S sites in vivianite potentially leads to the incorporation of Cd into the vivianite crystal structure (Yuan et al., 2018). This could occur through isomorphous substitution at the A-site Fe(II) or by forming a multidentate coordination structure with the vacancies and cationic sites in vivianite (Sun et al., 2020). The coordination structure, as modeled from EXAFS fitting results, includes two adjacent P atoms and neighboring A-site Fe atoms. Through geometry optimization and energy calculations of the reaction processes, it is revealed that forming a multidentate coordination structure is energetically more favorable (-189.5 eV) compared to isomorphous substitution (-154.7 eV). The abovementioned characterization results confirm that, upon reoxidation, the distribution of different Fe sites in vivianite remained unchanged from its initial state, yet Cd was integrated into the vivianite structure. This integration is attributed to the fact that, under six-coordination conditions, the atomic radius of Cd (1.52 Å) is substantially larger than that of Fe (1.26 Å), which hinders the formation of isomorphous crystals (Alam and Elzinga, 2023). However, the presence of large interstices within the vivianite lattice facilitates the accommodation of larger radius cations like Cd. It is considered that Cd establishes coordination with P and Fe predominantly through the Cd-O-P and Cd-O-Fe bonds, respectively, with both types of bonds converging at a shared O atom. The bidentate Cd-O-P bonds (CN = 2) play a more significant role than the Cd-O-Fe bonds (CN = 0.7) in integrating Cd into the vivianite framework.

The results derived from experimental and theoretical analyses provide solid evidence of the behavior and ultimate fate of S and Cd species during the sulfidation−reoxidation process, as depicted in Fig. 6c. In the absence of oxygen, S^{2-} actively participates in forming four-coordinated CdS precipitates with Cd^{2+} in the solution and concurrently incorporates into vivianite, binding with the positively charged Fe(II)-A sites and P sites. These solid-phase S^{2-} entities are prone to oxidation in the presence of oxygen. CdS precipitates undergo direct oxidation, dissolving and liberating SO_4^{2-}. The S sites in vivianite undergo a stepwise oxidation process, where electrons are donated from the 3p and 3s orbitals to O, thus reducing S electronegativity and consequently weakening the Fe-S and P-S bonds (Krest et al., 2015). The exothermic formation of new S-O bonds accelerates the oxidation of low-valence S sites in vivianite (Terranova et al., 2018). The complete electron stripping from the S orbitals results in the breakdown of Fe-S and P-S bonds, leading to the transformation of solid-phase S into SO_4^{2-}. This transformation creates defects in the spatial structure that facilitate Cd^{2+} immobilization. Consequently, Cd^{2+} species, which resist forming precipitates with the large ionic radius of SO_4^{2-}, do not dissolve into water upon reoxidation. Instead, they are sequestered within the vivianite matrix, stabilizing as solid-phase Cd through the Cd-O-P and Cd-O-Fe bonds.

4. Conclusions

This study demonstrates the beneficial synergistic relationship between S^{2-} and vivianite, showing that the sulfidation−reoxidation process markedly enhanced the capacity to immobilize cationic heavy metals such as Cd, Cu, and Zn. Molecular-level investigations, including Mössbauer spectroscopy, EXAFS studies, and DFT simulations, provide critical insights into the interactions between S^{2-}, vivianite, and Cd across various scenarios. It is observed that under anoxic (oxygen-free) conditions, S^{2-} directly sulfidized Fe(II) sites, which are located at the corners of the PO4 tetrahedron in vivianite (A sites). When the environment transitioned to aerobic (oxygen-rich) conditions, it became thermodynamically favorable for two adjacent Fe sites (A sites) and neighboring P atoms to coordinate with Cd through the Cd-O-Fe and Cd-O-P bonds, respectively. These findings challenge two prevailing perspectives in geochemistry and environmental chemistry: the perceived lesser effectiveness of vivianite in sequestering heavy metals (Hong et al., 2023; Wang et al., 2023a) and the assumption that reoxidation of metal sulfides results in the release of heavy metals (Huang et al., 2021a; Kong et al., 2018; Peltier et al., 2005). This research illuminates the influence of the Fe and S cycles, affected by redox condition fluctuations, on the natural environment's ability to accommodate harmful heavy metals. By leveraging structural similarities in a range of natural minerals and passivation materials, the immobilization of heavy metals becomes achievable (Brown et al., 1999). This understanding is crucial for developing a comprehensive model of elemental migration, spanning from individual molecules to the entire geosphere. In addition, these insights offer new approaches for developing strategies to control heavy metal pollution and enhance environmental remediation efforts.

CRediT authorship contribution statement

Zhangyi Xu: Writing – review & editing, Writing – original draft, Methodology, Investigation, Formal analysis, Data curation, Conceptualization. **Ziyuan Huang:** Investigation, Formal analysis, Data curation. **Han Li:** Visualization, Investigation, Data curation. **Shishu Zhu:** Validation, Methodology, Formal analysis. **Zhenchao Lei:** Validation, Formal analysis. **Chengshuai Liu:** Writing – review & editing, Supervision, Funding acquisition. **Fangyuan Meng:** Visualization, Data curation. **Jeng-Lung Chen:** Methodology, Formal analysis. **Tsung-Yi Chen:** Validation, Data curation. **Chunhua Feng:** Writing – review & editing, Writing – original draft, Supervision, Project administration, Funding acquisition, Conceptualization.

Declaration of competing interest

The authors declare that they have no known competing financial interests or personal relationships that could have appeared to influence the work reported in this paper.

Data availability

Data will be made available on request.

Acknowledgments

We gratefully acknowledge financial support from the National Key Research and Development Program of China (nos. 2020YFC1808502); the National Natural Science Foundation of China (nos. U21A2034 and 42025705); and the Special Support Plan for Innovation Teams of Guangdong Province, China (no. 2019BT02L218).

Supplementary materials

Supplementary material associated with this article can be found, in the online version, at doi:10.1016/j.watres.2024.122195.

References

Alam, K.M.N., Elzinga, E.J., 2023. Dynamics and mechanisms of Mn(II), Co(II), Ni(II), Zn (II), and Cd(II) sorption onto green rust sulfate. Environ. Sci. Technol. 57 (22), 8396–8405.

Bae, S., Sihn, Y., Kyung, D., Yoon, S., Eom, T., Kaplan, U., Kim, H., Schäfer, T., Han, S., Lee, W., 2018. Molecular identification of Cr(VI) removal mechanism on vivianite surface. Environ. Sci. Technol. 52 (18), 10647–10656.

Bogush, A.A., Leonova, G.A., Krivonogov, S.K., Bychinsky, V.A., Bobrov, V.A., Maltsev, A.E., Tikhova, V.D., Miroshnichenko, L.V., Kondratyeva, L.M., Kuzmina, A. E., 2022. Biogeochemistry and element speciation in sapropel from freshwater Lake Dukhovoe (East Baikal region, Russia). Appl. Geochem. 143, 10–38.

Brown, G.E., Foster, A.L., Ostergren, J.D., 1999. Mineral surfaces and bioavailability of heavy metals: a molecular-scale perspective. Proc. Natl. Acad. Sci. U. S. A. 96 (7), 3388–3395.

Chen, C., Kukkadapu, R.K., Lazareva, O., Sparks, D.L., 2017. Solid-phase Fe speciation along the vertical redox gradients in floodplains using XAS and Mössbauer spectroscopies. Environ. Sci. Technol. 51 (14), 7903–7912.
Cheng, D., Liao, W., Yuan, S., 2020. Effect of *in situ* generated iron oxyhydroxide coatings on FeS oxygenation and resultant hydroxyl radical production for contaminant degradation. Chem. Eng. J. 394 (3), 124–131.
Cosmidis, J., Benzerara, K., Morin, G., Busigny, V., Lebeau, O., Jézéquel, D., Noël, V., Dublet, G., Othmane, G., 2014. Biomineralization of iron-phosphates in the water column of Lake Pavin (Massif Central, France). Geochim. Cosmochim. Acta 126, 78–96.
Cutsail III, G.E., Banerjee, R., Zhou, A., Que Jr., L., Lipscomb, J.D., DeBeer, S, 2018. High-resolution extended X-ray absorption fine structure analysis provides evidence for a longer Fe···Fe distance in the Q intermediate of methane monooxygenase. J. Am. Chem. Soc. 140 (48), 16807–16820.
Delley, B.J., 1990. An all-electron numerical method for solving the local density functional for polyatomic molecules. J. Chem. Phys. 92 (1), 508–517.
Delley, B.J., 2000. From molecules to solids with the DMol3 approach. J. Chem. Phys. 113 (18), 7756–7764.
Dormann, J.L., Gasperin, M., Poullen, J.F., 1982. Etude structural de la seqence d'oxidation de la vivianite $Fe_3(PO_4)_2$ $8H_2O$. Bull. Soc. Fr. Mineral. 105, 147–160.
Dyar, M.D., Jawin, E.R., Breves, E., Marchand, G., Nelms, M., Lane, M.D., Mertzman, S. A., Bish, D.L., Bishop, J.L., 2014. Mössbauer parameters of iron in phosphate minerals: implications for interpretation of martian data. Am. Mineral. 99 (5–6), 914–942.
Eitel, E.M., Taillefert, M., 2017. Mechanistic investigation of Fe(III) oxide reduction by low molecular weight organic sulfur species. Geochim. Cosmochim. Acta 215, 173–188.
ElBelghitti, A., Boukhari, A., Holt, E.M., 1994. Cadmium iron(III) iron(II) diphosphate. Acta Crystallogr. 50 (11), 1648–1650.
Etique, M., Bouchet, S., Byrne, J.M., ThomasArrigo, L.K., Kaegi, R., Kretzschmar, R., 2021. Mercury Reduction by nanoparticulate vivianite. Environ. Sci. Technol. 55 (5), 3399–3407.
Frossard, E., Sinaj, S., Zhang, L.M., Morel, J.L., 1996. The fate of sludge phosphorus in soil-plant systems. Soil Sci. Soc. Am. 60 (4), 1248–1253.
Funke, H., Chukalina, M., Scheinost, A.C., 2007. A new FEFF-based wavelet for EXAFS data analysis. J. Synchrotron Radiat. 14 (5), 426–432.
He, L., Xie, L., Wang, D., Li, W., Fortner, J.D., Li, Q., Duan, Y., Shi, Z., Liao, P., Liu, C., 2019. Elucidating the role of sulfide on the stability of Ferrihydrite colloids under anoxic conditions. Environ. Sci. Technol. 53 (8), 4173–4184.
Hong, T., Wei, L., Li, Z., Wang, Y., Zhang, Q., Luo, L., Zhang, T., Li, R., Tang, Y., 2023. Exploring the acid–base surface properties of vivianite crystals in aqueous solution. Surf. Interface Anal. 55 (12), 871–879.
Huang, H., Ji, X.B., Cheng, L.Y., Zhao, F.J., Wang, P., 2021a. Free radicals produced from the oxidation of ferrous sulfides promote the remobilization of cadmium in paddy soils during drainage. Environ. Sci. Technol. 55 (14), 9845–9853.
Huang, M., Liu, C., Cui, P., Wu, T., Feng, X., Huang, H., Zhou, J., Wang, Y., 2021b. Facet-dependent photoinduced transformation of cadmium sulfide (CdS) nanoparticles. Environ. Sci. Technol. 55 (19), 13132–13141.
Huang, Z., Ma, H., Liu, C., Meng, F., Lee, J.F., Lin, Y.J., Yi, X., Dang, Z., Feng, C., 2023. A coupled electrochemical process for schwertmannite recovery from acid mine drainage: important roles of anodic reactive oxygen species and cathodic alkaline. J. Hazard. Mater. 451, 131075.
Karna, R.R., Noerpel, M.R., Nelson, C., Elek, B., Herbin-Davis, K., Diamond, G., Bradham, K., Thomas, D.J., Scheckel, K.G., 2021. Bioavailable soil Pb minimized by *in situ* transformation to plumbojarosite. Proc. Natl. Acad. Sci. U. S. A. 118 (3), e2020315117.
Kong, L., Peng, X., Hu, X., Chen, J., Xia, Z., 2018. UV-Light-Induced aggregation of arsenic and metal sulfide particles in acidic wastewater: the role of free radicals. Environ. Sci. Technol. 52 (18), 10719–10727.
Krest, C.M., Silakov, A., Rittle, J., Yosca, T.H., Onderko, E.L., Calixto, J.C., Green, M.T., 2015. Significantly shorter Fe–S bond in cytochrome P450-I is consistent with greater reactivity relative to chloroperoxidase. Nat. Chem. 7 (9), 696–702.
Li, W., Joshi, S.R., Hou, G., Burdige, D.J., Sparks, D.L., Jaisi, D.P., 2015. Characterizing phosphorus speciation of chesapeake bay sediments using chemical extraction, 31P NMR, and X-ray absorption fine structure spectroscopy. Environ. Sci. Technol. 49 (1), 203–211.
Liang, S., Zhu, L., Hua, J., Duan, W., Yang, P.T., Wang, S.L., Wei, C., Liu, C., Feng, C., 2020. Fe^{2+}/HClO reaction produces $Fe^{IV}O^{2+}$: an enhanced advanced oxidation process. Environ. Sci. Technol. 54 (10), 6406–6414.
Liu, R., Zhao, D, 2007. Reducing leachability and bioaccessibility of lead in soils using a new class of stabilized iron phosphate nanoparticles. Water Res. 41, 2491–2502.
Martinie, R.J., Blaesi, E.J., Krebs, C., Bollinger Jr., J.M., Silakov, A., Pollock, C.J, 2017. Evidence for a Di-μ-oxo diamond core in the Mn(IV)/Fe(IV) activation intermediate of ribonucleotide reductase from chlamydia trachomatis. J. Am. Chem. Soc. 139 (5), 1950–1957.
Momma, K., Izumi, F., 2008. VESTA: a three-dimensional visualization system for electronic and structural analysis. J. Appl. Crystallogr. 41 (3), 44–45.
Muehe, E.M., Morin, G., Scheer, L., Pape, P.L., Esteve, I., Daus, B., Kappler, A., 2016. Arsenic(V) incorporation in vivianite during microbial reduction of Arsenic(V)-bearing biogenic Fe(III) (oxyhydr)oxides. Environ. Sci. Technol. 50 (5), 2281–2291.
Mueller, W.J., Loeffler, G., 1933. Zur kenntnis der faerbung von gefaelltem cadmiumsulfid. Angew. Chem. 46, 538–539 (German Edition).
Pan, Y., Ye, H., Yang, Y., Yang, C., Li, X., Ma, T., Dang, Z., Lu, G., 2023. Transport and fate of Cu and Cd in contaminated paddy soil under acid mine drainage. J. Environ. Manag. 334 (10), 117–127.
Peltier, E., Dahl, A.L., Gaillard, J.F., 2005. Metal Speciation in anoxic sediments: when sulfides can be construed as oxides. Environ. Sci. Technol. 39 (1), 311–316.
Pinto, H.P., Michalkova, A., Leszczynski, J., 2014. First-principles studies of paramagnetic vivianite $Fe_3(PO_4)_2{\cdot}8H_2O$ surfaces. J. Phys. Chem. C 118 (12), 6110–6121.
Qin, L., Wang, L., Zhao, S., Sun, X., Yu, L., Wang, M., Chen, S., 2022. A new insight into Cd reduction by flooding in paddy soil: the different dominant roles of Fe and S on Cd immobilization under fluctuant pe + pH conditions. Sci. Total Environ. 847, 157–169.
Qiu, J., Hou, X., Ren, Y., Liu, C., Meng, F., Lee, J.F., Lin, Y.J., Huang, Z., Ma, H., Shi, Z., Feng, C., 2023. Photoinduced transformation of ferrihydrite in the presence of aqueous sulfite and its influence on the repartitioning of Cd. Water Res. 231, 11–24.
Rastegari, M., Karimian, N., Johnston, S.G., Doherty, S.J., Hamilton, J.L., Choppala, G., Hosseinpour Moghaddam, M., Burton, E.D., 2022. Antimony(V) incorporation into schwertmannite: critical insights on antimony retention in acidic environments. Environ. Sci. Technol. 56 (24), 17776–17784.
Ravel, B., Newville, M., 2005. ATHENA, ARTEMIS, HEPHAESTUS: data analysis for X-ray absorption spectroscopy using IFEFFIT. J. Synchrotron Radiat. 12 (4), 537–541.
Rothe, M., Kleeberg, A., Hupfer, M., 2016. The occurrence, identification and environmental relevance of vivianite in waterlogged soils and aquatic sediments. Earth Sci. Rev. 158 (3), 51–64.
Saracanlao, R.J., Saelens, T., Voegelin, A., Smolders, E., Everaert, M., 2024. Recycled iron phosphates: a new phosphorus fertilizer for paddy rice. Environ. Sci. Technol. 58 (21), 9250–9260.
Schröder, C., Wan, M., Butler, I.B., Tait, A., Peiffer, S., McCammon, C.A., 2020. Identification of mackinawite and constraints on its electronic configuration using Mössbauer spectroscopy. Minerals 10 (12), 1090.
Sun, Q., Burton, E.D., Si, D., Fan, T., Cheng, H., Yu, Z., Shao, X., Cui, P., Wang, Y., 2023. Coupling of dissolved organic matter molecular fractionation with iron and sulfur transformations during sulfidation–reoxidation cycling. Environ. Sci. Technol. 57 (43), 16327–16339.
Sun, Q., Cui, P., Wu, S., Liu, C., Fan, T., Alves, M.E., Cheng, H., Huang, M., Zhou, D., Wang, Y., 2020. Role of reduced sulfur in the transformation of Cd(II) immobilized by δ-MnO_2. Environ. Sci. Technol. 54 (23), 14955–14963.
Szeto, K.C., Jones, Z.R., Merle, N., Rios, C., Gallo, A., Le Quemener, F., Delevoye, L., Gauvin, R.M., Scott, S.L., Taoufik, M., 2018. A strong support effect in selective propane dehydrogenation catalyzed by $Ga(i\text{-}Bu)_3$ grafted onto γ-Alumina and silica. ACS Catal. 8 (8), 7566–7577.
Tagliabue, A., Bowie, A.R., Boyd, P.W., Buck, K.N., Johnson, K.S., Saito, M.A., 2017. The integral role of iron in ocean biogeochemistry. Nature 543 (7643), 51–59.
Terranova, U., Mitchell, C., Sankar, M., Morgan, D.J., Leeuw, N.H.D., 2018. Initial oxygen incorporation in the prismatic surfaces of troilite FeS. J. Phys. Chem. C 122 (24), 94–97.
Veeramani, H., Alessi, D.S., Suvorova, E.I., Lezama-Pacheco, J.S., Stubbs, J.E., Sharp, J. O., Dippon, U., Kappler, A., Bargar, J.R., Bernier-Latmani, R., 2011. Products of abiotic U(VI) reduction by biogenic magnetite and vivianite. Geochim. Cosmochim. Acta 75, 2512–2528.
Wang, P., Zuo, W., Zhu, W., Wang, S., Li, B., Jiang, Y., Wang, G., Tian, Y., Zhang, Y., 2023a. Deciphering the interaction of heavy metals with Geobacter-induced vivianite recovery from wastewater. Water Res. 24, 12–21.
Wang, Q., Wang, J., Wang, X., Kumar, N., Pan, Z., Peiffer, S., Wang, Z., 2023b. Transformations of ferrihydrite–extracellular polymeric substance coprecipitates driven by dissolved sulfide: interrelated effects of carbon and sulfur loadings. Environ. Sci. Technol. 57 (10), 4342–4353.
Wang, S., Lu, Q., Liang, Z., Yu, X., Lin, M., Mai, B., Qiu, R., Shu, W., He, Z., Wall, J.D., 2023c. Generation of zero-valent sulfur from dissimilatory sulfate reduction in sulfate-reducing microorganisms. Proc. Natl. Acad. Sci. U. S. A. 120 (20), e2220725120.
Wilfert, P., Mandalidis, A., Dugulan, A.I., Goubitz, K., Korving, L., Temmink, H., Witkamp, G.J., Van Loosdrecht, M.C.M., 2016. Vivianite as an important iron phosphate precipitate in sewage treatment plants. Water Res. 104, 449–460.
Wu, Y., Wang, C., Wang, S., An, J., Liang, D., Zhao, Q., Tian, L., Wu, Y., Wang, X., Li, N., 2021. Graphite accelerate dissimilatory iron reduction and vivianite crystal enlargement. Water Res. 189, 116663.
Xiong, Y., Guilbaud, R., Peacock, C.L., Cox, R.P., Canfield, D.E., Krom, M.D., Poulton, S. W., 2019. Phosphorus cycling in Lake Cadagno, Switzerland: a low sulfate euxinic ocean analogue. Geochim. Cosmochim. Acta 251, 116–135.
Yiming, S., David, J., Shikun, S., Xuefei, Z., Hongying, Z., 2018. Enhanced oxidative and adsorptive removal of diclofenac in heterogeneous fenton-like reaction with sulfide modified nanoscale zerovalent iron. Environ. Sci. Technol. 52 (3), 6466–6475.
Yin, Y., Shi, L., Li, W., Li, X., Wu, H., Ao, Z., Tian, W., Liu, S., Wang, S., Sun, H., 2019. Boosting fenton-like reactions via single atom Fe catalysis. Environ. Sci. Technol. 53 (19), 11391–11400.
Yu, Q., Fein, J.B., 2015. The effect of metal loading on Cd adsorption onto Shewanella oneidensis bacterial cell envelopes: the role of sulfhydryl sites. Geochim. Cosmochim. Acta 167, 1–10.
Yuan, B., Egner, T.K., Venditti, V., Cademartiri, L., 2018. Sustainable scalable synthesis of sulfide nanocrystals at low cost with an ionic liquid sulfur precursor. Nat. Commun. 9 (1), 4078.
Zhang, C., Cheng, X., Wang, M., Ma, J., Collins, R., Kinsela, A., Zhang, Y., Waite, T.D., 2021. Phosphate recovery as vivianite using a flow-electrode capacitive desalination (FCDI) and fluidized bed crystallization (FBC) coupled system. Water Res. 194, 116939.
Zhou, W., Zhou, J., Feng, X., Wen, B., Zhou, A., Liu, P., Sun, G., Zhou, Z., Liu, X., 2023. Antimony isotope fractionation revealed from EXAFS during adsorption on Fe (oxyhydr)oxides. Environ. Sci. Technol. 57 (25), 9353–9361.